Journal of Materials Chemistry C

ROYAL SOCIETY OF CHEMISTRY

PAPER

View Article Online
View Journal | View Issue

Cite this: J. Mater. Chem. C, 2021, 9, 10749

Dysprosium–dianthracene framework showing thermo-responsive magnetic and luminescence properties†

Qian Zou,[a] Tao Shang,[b] Xin-Da Huang,[a] Qing-Qing Guo,[a] Jia-Ge Jia,[a] Song-Song Bao, *[a] Yi-Quan Zhang*[b] and Li-Min Zheng *[a]

Received 5th March 2021,
Accepted 6th May 2021

DOI: 10.1039/d1tc01027a

rsc.li/materials-c

Metal–organic frameworks showing stimuli-responsive magneto-optical properties are of intensive current interest for potential applications in spintronics and molecular devices. By incorporating a thermo-responsive dianthracene component into a lanthanide phosphonate framework, we successfully obtained compounds $Ln_2(amp_2H_2)_2(C_2O_4)(H_2O)_2{\cdot}xH_2O$ (**MDAF-4Ln**, Ln = Dy, x = 10; Gd, x = 9; Er, x = 7; and amp_2H_4 = pre-photodimerized 9-anthrylmethylphosphonic acid). These compounds are isostructural showing three-dimensional open framework structures composed of Ln-chains and dianthracence linkages. Within the chain, the dimers of $\{Ln_2O_2(OPO)_2\}$ are connected by oxalate anions. The MOFs generate channels along the a-axis which are hydrophilic lined with protonated phosphonate moieties, and hence exhibit high affinity towards adsorption of water and ammonia. Thermogravimetric analysis and differential scanning calorimetry (DSC) measurements revealed that **MDAF-4Ln** experienced two consecutive phase transitions: first, the loss of all lattice and coordinated water molecules and then, the dissociation of $amp_2H_2^{2-}$. Detailed studies on **MDAF-4Dy** demonstrated that the thermo-induced structural transformations were accompanied by significant changes in its single-molecule magnetic behavior and luminescence properties.

Introduction

Metal–organic frameworks (MOFs) with responsive magneto-optical bifunctions are highly desired not only for developing multifunctional materials but also for applications in spintronics and molecular devices.[1] Lanthanide-based MOFs are appealing in this context because lanthanide ions possess significant single-ion magnetic anisotropy arising from strong spin–orbit coupling and crystal-field effects.[2] They also exhibit well-resolved characteristic photoluminescence upon sensitization by an organic antenna.[3]

The intrinsic strong magnetic anisotropy of lanthanide ions has enabled the construction of numerous single-molecule magnets (SMMs) based on lanthanide complexes,[4,5] especially the mononuclear species with highly symmetric electrostatic environments,[6–10] the blocking temperature of which reached near or even above the temperature of liquid nitrogen.[11–13] By contrast, the magnetic performance of Ln-MOFs is far less exciting.[14] Apart from the difficulties in controlling the coordination geometries of lanthanide ions in MOFs, organizing lanthanide ions in the framework structure often leads to non-parallel arrangements of the magnetic easy-axes which largely reduce the overall magnetic anisotropy.[15] Therefore, only few Ln-MOFs were reported showing SMM behaviour under zero external field (Table S1, ESI†).[16–28] Nevertheless, Ln-MOFs have their own advantages over mononuclear or cluster species. They could create arrays of SMM species that are well separated in space. The structural rigidity of MOFs has the advantage of minimizing the spin-phonon fast-relaxation mechanism, which is important for high-performance SMMs.[28] Moreover, the magnetic dynamics of Ln-SMMs are very sensitive to subtle structural changes including the coordination geometry, crystal packing and hydrogen bond network.[29] The magnetic properties of Ln-MOFs can be tuned by changing the guest molecules inside the pore and modifying the organic linkers in the framework. Indeed, Ln-MOFs with their SMM behaviour responsive to guest exchange and de-solvation have been described.[23–27] Regarding the organic linkers, Yamashita and co-workers reported a 2D Dy-dithienylethane compound showing light-triggered changes of SMM properties due to the ring-open and ring-close isomerism.[30]

Ln-MOFs exhibiting luminescence and SMM bifunctions were much less explored.[22,23,31–33] Simultaneous manipulation

[a] State Key Laboratory of Coordination Chemistry, School of Chemistry and Chemical Engineering, Collaborative Innovation Centre of Advanced Microstructures, Nanjing University, Nanjing 210023, P. R. China. E-mail: lmzheng@nju.edu.cn, baososo@nju.edu.cn

[b] Jiangsu Key Laboratory for NSLSCS, School of Physical Science and Technology, Nanjing Normal University, Nanjing 210023, China. E-mail: zhangyiquan@njnu.edu.cn

† Electronic supplementary information (ESI) available. CCDC 2065604–2065606. For ESI and crystallographic data in CIF or other electronic format see DOI: 10.1039/d1tc01027a

of both luminescence and SMM behaviour in Ln-MOFs remains to be a formidable challenge since the characteristic luminescence of lanthanide ions is insensitive to external stimuli. The only example, as far as we are aware, was given by Ohkoshi, Chorazy and co-workers.[26] They found that the coordination geometry of Dy^{III} in a cyanide-bridged $Dy^{III}Co^{III}$ framework changed upon dehydration from the D_{4d} to D_{3h} symmetry. This change caused the switch-on of SMM properties and the shift of luminescent colour from nearly white to deep yellow.

Our strategy to construct Ln-MOFs with switchable magneto-optical bifunctions uses stimuli-responsive organic ligands as linkers in the skeleton. To this end, dianthracene derivatives are ideal candidates because they can de-dimerize upon thermal treatment or UV light irradiation with change in luminescence.[34–37] Considering that the organophosphonate ligands have strong binding capabilities toward lanthanide ions forming MOFs embedding lanthanide clusters, chains or layers,[38–46] herein, we choose a pre-photodimerized 9-anthrylmethylphosphonic acid (amp_2H_4) as a linker to build new Ln-MOFs that possess magneto-optical bifunctions responsive to external stimuli. Compounds $Ln_2(amp_2H_2)_2(C_2O_4)(H_2O)_2{\cdot}xH_2O$ (**MDAF-4Ln**, Ln = Dy, x = 10; Gd, x = 9; Er, x = 7; MDAF means Metal DiAnthracene Framework) were successfully isolated under hydrothermal conditions. They are isostructural showing three-dimensional open framework structures composed of Ln-chains and dianthracence linkages. Within the chain, the dimers of $\{Ln_2O_2(OPO)_2\}$ are bridged by oxalate anions. Magnetic studies revealed dominant antiferromagnetic (AF) exchange coupling between the magnetic centres within the chain, which was supported by theoretical calculations. Interestingly, **MDAF-4Dy** showed slow magnetization relaxation under zero static field, characteristic of the SMM behaviour. Theoretical calculations confirmed that the ground Kramers doublet (KD) of an individual Dy^{III} fragment is mostly composed of the $m_J = \pm 15/2$ state. For **MDAF-4Er**, field-induced SMM behaviour was observed. Compound **MDAF-4Dy** was further subjected to a detailed magnetic and luminescence study upon thermal treatment. The results demonstrated that it experienced thermo-driven two consecutive phase transitions: first, the loss of all lattice and coordination water molecules and then, the dissociation of $amp_2H_2^{2-}$. The phase transitions were accompanied by dramatic changes in luminescence and magnetic dynamics. To our knowledge, only one Ln-dianthracene MOF was previously reported in the literature without concerning the magnetic or luminescence properties.[35] Therefore, compounds **MDAF-4Ln** are the first examples of Ln-dianthracene MOFs with magneto-optical bifunctions. Particularly, **MDAF-4Dy** is the first example of Ln-dianthracene MOFs showing thermo-responsive magnetic dynamics and luminescence properties.

Experimental section

Materials and instrumentation

Photodimerized 9-anthrylmethylphosphonic acid (amp_2H_4) was synthesized according to the literature method.[36] All the starting materials were obtained from commercial sources and used without further purification. Elemental analysis for C and H was performed using a PerkinElmer 240C elemental analyzer. The infrared spectra were recorded using a Bruker Tensor 27 spectrometer in the region of 4000–400 cm^{-1}. Thermogravimetric analysis was performed using a Mettler Toledo TGA/DSC 1 instrument in the range of 30–600 °C under a nitrogen flow at a heating rate of 5 °C min^{-1}. Differential scanning calorimetry (DSC) measurements were conducted using a METTLER DSC823e/200 under N_2 atmosphere. The powder XRD patterns were recorded using a BRUKER D8 Advance X-ray diffractometer with Cu Kα radiation (λ = 1.5406 Å). Single-crystal diffraction data were collected at 193 K using a Bruker D8 Venture. The UV-vis spectra were recorded using a PerkinElmer Lambda 950 UV-vis spectrometer. The steady fluorescence spectra were obtained using a PerkinElmer Spectrofluorometer LS55. Time-resolved fluorescence and quantum yield were measured using a Fluorolog TCSPC spectrofluorometer (Horiba Scientific). The ac and dc magnetization data were obtained on polycrystalline samples using Quantum Design VSM SQUID magnetometers. The data were corrected for the diamagnetic contributions of the compounds obtained from Pascal's constants and for the sample holders.[47]

Synthesis of $Ln_2(amp_2H_2)_2(C_2O_4)(H_2O)_2{\cdot}xH_2O$ (MDAF-4Ln). Compounds **MDAF-4Ln** (Ln = Dy, Gd, Er) were synthesized similarly except using a different $LnCl_3{\cdot}6H_2O$. A typical procedure for the synthesis of $Dy_2(amp_2H_2)_2(C_2O_4)(H_2O)_2{\cdot}10H_2O$ (**MDAF-4Dy**) is given below. A mixture of amp_2H_4 (13.6 mg, 0.025 mmol), $DyCl_3{\cdot}6H_2O$ (18.8 mg, 0.05 mmol) and $H_2C_2O_4$ (3.1 mg, 0.025 mmol) in 6 mL of water was sealed in a Teflon-lined autoclave and heated under autogenous pressure at 95 °C for 2 days. After cooling to room temperature, rhombic colourless crystals of **MDAF-4Dy** were collected, washed with water and then air-dried. The purity was confirmed by the PXRD measurement (Fig. S1 in ESI†). Yield: 47.3% (based on amp_2H_4). Elemental anal. calcd (%) for $Dy_2C_{62}H_{72}O_{28}P_4$: C, 44.37; H, 4.08. Found (%): C, 44.19; H, 4.16. IR (KBr, cm^{-1}): 3606(m), 3428(m), 3062(w), 3033(w), 2923(w), 1643(s), 1477(m), 1452(m), 1427(w), 1346(w), 1313(s), 1255(w), 1236(w), 1190(m), 1126(m), 1060(s), 1016(m), 966(w), 935(w), 798(w), 767(m), 733(w), 692(m), 646(m), 619(w), 570(m), 536(m), 486(w), 443(m).

For $Gd_2(amp_2H_2)_2(C_2O_4)(H_2O)_2{\cdot}9H_2O$ (**MDAF-4Gd**), yield: 40.5% (based on amp_2H_4). Elemental anal. calcd (%) for $Gd_2C_{62}H_{70}O_{27}P_4$: C, 44.17; H, 4.19. Found (%): C, 44.35; H, 4.24. IR (KBr, cm^{-1}): 3605(m), 3428(m), 3063(w), 3033(w), 2924(w), 1637(s), 1477(m), 1452(m), 1427(w), 1348(w), 1312(s), 1255(w), 1236(w), 1189(m), 1126(m), 1061(s), 1015(m), 966(w), 935(w), 799(w), 768(m), 734(w), 691(m), 646(m), 619(w), 571(m), 526(m), 486(w), 448(m).

For $Er_2(amp_2H_2)_2(C_2O_4)(H_2O)_2{\cdot}7H_2O$ (**MDAF-4Er**), yield: 42.1% (based on amp_2H_4). Elemental anal. calcd (%) for $Er_2C_{62}H_{66}O_{25}P_4$: C, 44.60; H, 3.98. Found (%): C, 44.52; H, 3.66. IR (KBr, cm^{-1}): 3606(m), 3428(m), 3062(w), 3033(w), 2924(w), 1637(s), 1477(m), 1452(m), 1427(w), 1350(w), 1313(s), 1255(w), 1236(w), 1190(m), 1126(m), 1060(s), 1016(m), 966(w), 935(w), 798(w), 767(m), 733(w), 691(m), 646(m), 619(w), 570(m), 528(m), 487(w), 445(m).

Single-crystal structure determination

Suitable single crystals of **MDAF-4Ln** were selected and mounted on the loops. The single-crystal data sets were collected at 193 K using a Bruker D8 Venture diffractometer with Mo-K_α radiation (λ = 0.71073 Å) for **MDAF-4Dy**, **MDAF-4Gd** and **MDAF-4Er**. The numbers of collected and observed independent [$I > 2\sigma(I)$] reflections were 12 449 and 6160 (R_{int} = 0.0407) for **MDAF-4Dy**, 10 334 and 5906 (R_{int} = 0.0357) for **MDAF-4Gd**, and 10656 and 5780 (R_{int} = 0.0591) for **MDAF-4Er**, respectively. The data were integrated using the Siemens SAINT program,[48] and adsorption corrections were applied. The structures were solved by a direct method and refined on F^2 by full-matrix least-squares using SHELXTL.[49] All non-hydrogen atoms were refined using anisotropic thermal parameters. All hydrogen atoms bound to carbon were refined isotropically in the riding mode. The hydrogen atoms of the coordinated water molecule (O1W) were detected *via* experimental electron density. The O–H bond distances and the H–O–H angle were restricted, and then, the water molecule was made into a rigid group using the AFIX 6 instruction. The O3 and O6 atoms from the phosphonate groups are protonated due to the elongated P–O bonds and charge balance. The AFIX 83 instruction was used to add the hydrogen atoms to the O3 and O6 atoms. In all cases, residual electron densities in the solvent-accessible void were treated with the PLATON/SQUEEZE program[50] owing to the heavily disordered solvent molecules. The solvent-accessible voids calculated from the SQUEEZE results are 429 (**MDAF-4Dy**), 418 (**MDAF-4Gd**), and 398 (**MDAF-4Er**) Å^3 per unit, which can amount to around ten lattice water molecules (*ca.* 40 Å^3 per H_2O).

Results and discussion

Crystal Structure of MDAF-4Ln

Compounds **MDAF-4Ln** are isostructural as confirmed by their PXRD patterns and single crystal data (Table 1, Fig. S1, ESI†). Hence, **MDAF-4Dy** is selected as a representative for a detailed structural description. $Dy_2(amp_2H_2)_2(C_2O_4)(H_2O)_2{\cdot}10H_2O$ (**MDAF-4Dy**) crystallises in the triclinic space group $P\bar{1}$ and the asymmetric unit consists of one Dy^{III} ion, two kinds of $amp_2H_2^{2-}$ ligands (each with half occupancy), 0.5 $C_2O_4^{2-}$, one coordinated water molecule and five lattice water molecules (Fig. S3, ESI†). The lattice water molecules were heavily disordered and hence were treated with the PLATON/SQUEEZE program. The number of lattice water molecules was determined based on elemental and thermal analyses. As shown in Fig. 1a, the Dy^{III} ion is eight-coordinated by five O atoms from four $amp_2H_2^{2-}$ ligands (O1A, O2A, O2, O4A, and O5), two O atoms from the chelated $C_2O_4^{2-}$ (O7, O8B), and one O atom from the coordinated water molecule (O1W). The Dy–O bond distances are in the range from 2.288(3) to 2.568(3) Å, and the O–Dy–O bond angles vary from 59.03(10) to 152.38(11)° (Table S2, ESI†). The geometry of the $\{DyO_8\}$ core is close to a distorted triangular dodecahedron with a D_{2d} symmetry, according to the continuous shape measure (CShM = 0.944)[51] analysis (Table S3, ESI†).

Two crystallographically different $amp_2H_2^{2-}$ ligands are found. One serves as a hexadentate ligand with each phosphonate group providing two oxygen donors (O1, O2) to chelate and bridge the Dy atoms (Scheme 1a). The other acts as a tetradentate ligand with each phosphonate group offering two oxygen donors (O4 and O5) to bridge the Dy atoms (Scheme 1b). The remaining phosphonate oxygen atoms (O3 and O6) are protonated. Consequently, the equivalent Dy atoms are linked by two μ_3-O2 and two O4–P2–O5 units forming $\{Dy_2O_2(OPO)_2\}$ dimers (Fig. 1a). These dimers are connected by oxalate ligands forming infinite chains running along the *a*-axis (Fig. 1b). The Dy···Dy distances over the μ_3-O2 and oxalate bridges within the chain are 3.891 and 6.169 Å, respectively. The dimers of $\{Dy_2O_2(OPO)_2\}$ are also connected by dianthracene groups, forming layers in the *bc* plane which contain rhombic windows composed of four $\{Dy_2O_2(OPO)_2\}$ dimers and four $amp_2H_2^{2-}$ ligands (Fig. 1c). The shortest Dy···Dy distance over the dianthracene ligand is 13.742 Å. The layers are cross-linked by oxalate ligands into a 3D open framework structure with channels generated along the *a*-axis (Fig. 1d). The lattice water molecules reside in the channels. Notably, all the protonated phosphonate oxygen atoms line on the channel wall.

Compounds **MDAF-4Gd** and **MDAF-4Er** also crystallize in the triclinic system space group $P\bar{1}$ (Table 1). They show similar 3D framework structures composed of Ln-chains and $amp_2H_2^{2-}$ linkers. The unit cell volume follows the order: **MDAF-4Gd** > **MDAF-4Dy** > **MDAF-4Er**, attributed to the lanthanide contraction effect. The Ln–O distances and O–Ln–O angles are in the ranges of 2.330(3)–2.578(3) Å and 58.67(10)–152.41(11) ° for **MDAF-4Gd**, and 2.275(4)–2.534(4) Å and 59.72(14)–151.64(14) ° for **MDAF-4Er**, respectively (Table 2).

It is worth mentioning that a few lanthanide oxalatophosphonates with 3D framework structures were previously reported. They are composed of Ln-oxalate chains[52–54] or layers with phosphonate linkers,[55,56] or lanthanide phosphonate layers with oxalate pillars.[57] These structures are completely different from those of **MDAF-4Ln**, where the lanthanide chains containing $\{Ln_2O_2(OPO)_2\}$ dimers and oxalate linkages are isolated by the bulky dianthracene groups. Hence, **MDAF-4Ln**

Table 1 Crystallographic data for **MDAF-4Dy**, **MDAF-4Gd** and **MDAF-4Er**

	MDAF-4Dy	MDAF-4Gd	MDAF-4Er
Empirical formula	$C_{31}H_{26}DyO_9P_2$	$C_{31}H_{26}GdO_9P_2$	$C_{31}H_{26}ErO_9P_2$
Temperature (K)	193(2)	193(2)	193(2)
F_W	766.96	761.71	771.72
Crystal system	Triclinic	Triclinic	Triclinic
Space group	$P\bar{1}$	$P\bar{1}$	$P\bar{1}$
a (Å)	9.5729(6)	9.6423(8)	9.4986(19)
b (Å)	13.826(1)	13.8366(13)	13.736(3)
c (Å)	14.8032(10)	14.8249(13)	14.760(3)
α (°)	63.398(2)	63.687(2)	63.610(5)
β (°)	75.488(2)	75.327(2)	75.449(6)
γ (°)	88.549(2)	88.631(3)	88.768(6)
V (Å^3)	1687.4 (2)	1706.2(3)	1660.8 (6)
Z	2	2	2
ρ_{calcd} (g cm^{-3})	1.509	1.483	1.543
F (000)	760.0	756.0	764.0
Goodness of fit	1.024	1.037	1.032
R_1, wR_2 [$I > 2\sigma(I)$][a]	0.0334, 0.0732	0.0358, 0.0820	0.0406, 0.1011
R_1, wR_2 (all data)[a]	0.0413, 0.0771	0.0432, 0.0847	0.0458, 0.1041
CCDC number	2065604	2065605	2065606

[a] $R_1 = \Sigma||F_o| - |F_c||/\Sigma|F_o|$, w$R_2 = [\Sigma w(F_o^2 - F_c^2)^2/\Sigma w(F_o^2)^2]^{1/2}$.

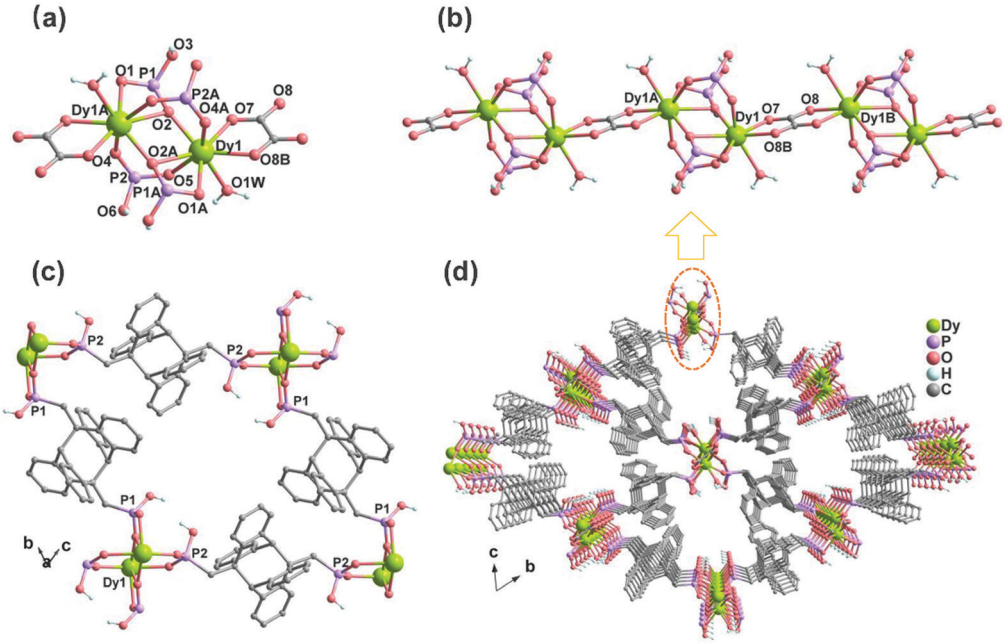

Fig. 1 Crystal structure of **MDAF-4Dy**. (a) Dimeric units with atomic numbering scheme; (b) a fragment of the chain composed of dysprosium dimeric units and oxalate linkages; (c) rhombic window of the Dy_2-diantracene layer; (d) open framework structure viewed along the *a*-axis. The disordered lattice water molecules are squeezed. All H atoms except those in coordinated water and phosphonate oxygen atoms are omitted for clarity.

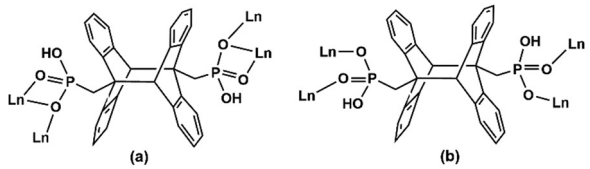

Scheme 1 Coordination modes of $amp_2H_2^{2-}$.

provide a new type of structure among lanthanide oxalatophosphonates. In addition, this structure is also distinct from the known Ln-dianthracene MOF (CD-MOF-161)[35] in which dimers of $\{Yb_2O(OCO)_2\}$ are interconnected by dianthracene dicarboxylate linkers.

Gas sorption properties

Knowing that the structures of **MDAF-4Ln** are porous with the pore-walls lined with hydrophilic P–OH moieties, we conjecture that the activated sample of **MDAF-4Ln** would show affinity to alkaline gas. To validate this assumption, **MDAF-4Dy**, activated at 100 °C under vacuum for 4 h, was chosen for gas sorption measurements including N_2, H_2, CO_2, NH_3 and H_2O. The N_2 adsorption/desorption at 77 K showed a type II isotherm with a loading of 3.98 $cm^3\ g^{-1}$ at P/P_0 = 0.98 (Fig. S4, ESI†), indicating that the interactions between nitrogen and the framework are very weak. The activated **MDAF-4Dy** can also adsorb H_2 at 77 K with hysteresis, but the capacities were low, with the uptake of 1.16 $cm^3\ g^{-1}$ at P/P_0 = 0.98 (Fig. S4, ESI†). Similarly, the CO_2 adsorption at 298 K was not high with a maximum uptake of 26.68 $cm^3\ g^{-1}$ at P/P_0 = 0.98. By contrast, a rapid and remarkably enhanced adsorption was observed for NH_3 at 298 K with the uptakes of 78.37 $cm^3\ g^{-1}$ (5.99 mol mol^{-1}) at P/P_0 = 0.02 and 129.07 $cm^3\ g^{-1}$ (5.76 mmol g^{-1}, 9.87 mol mol^{-1}) at P/P_0 = 0.98 (Fig. 2). The adsorption capacity of NH_3 is about 5 times higher than that of CO_2 at 298 K and is comparable to those found for other MOFs.[58] The strong adsorption capability of **MDAF-4Dy** toward ammonia may be explained by favourable interaction between alkaline NH_3 and acidic P–OH on the channel walls,

Table 2 Selected structural parameters for compounds **MDAF-4Ln**

	MDAF-4Dy	MDAF-4Gd	MDAF-4Er
C–C (central) [Å]	1.609, 1.636	1.613, 1.651	1.608, 1.642
Ln–O (P) [Å]	2.288–2.568	2.330–2.578	2.275–2.534
Ln–O ($C_2O_4^{2-}$) [Å]	2.352, 2.404	2.375, 2.431	2.320, 2.389
Ln–O (H_2O) [Å]	2.446	2.461	2.418
O–Ln–O (°)	59.03–152.38	58.67–152.41	59.72–151.64
Ln–O–Ln (°)	105.92	106.17	107.28
Ln···Ln (within dimer) [Å]	3.891	3.929	3.876
Ln···Ln (over dimers) [Å]	6.169	6.222	6.114
Ln···Ln (over $amp_2H_2^{2-}$) [Å]	13.742–15.595	13.773–15.651	13.645–15.568

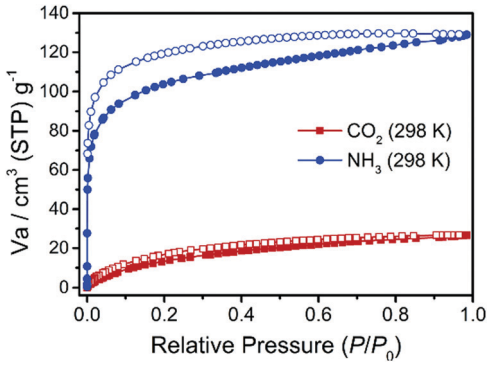

Fig. 2 Adsorption (filled) and desorption (open) isotherms of CO_2 and NH_3 at 298 K for **MDAF-4Dy**.

which is supported by the significant hysteresis of the ammonia adsorption/desorption isotherm. After desorption, there remained 68.31 cm^3 g^{-1} (5.22 mol mol^{-1}) of ammonia at P/P_0 = 0.001. This value is only slightly lower than the expected value of 6.0 mol mol^{-1} if the four P–OH groups per molecular formula are each strongly hydrogen-bonded to NH_3 and the two vacant sites of the Dy atoms are also filled with NH_3.

Significant hysteresis was also observed for water isotherm. In this case, the adsorption curve shows a gradual increase below P/P_0 = 0.09, and then a sharp increase until P/P_0 = 0.12, indicating a "gate opening" effect. The total adsorption capacity at P/P_0 = 1.01 is 158.24 cm^3 g^{-1} (or 12.10 mmol mmol^{-1}) (Fig. S5, ESI†), in agreement with the presence of two coordinated and ten lattice water molecules in the pristine compound. PXRD measurements confirmed that the original structure of **MDAF-4Dy** was maintained after activation and adsorption/desorption measurements (Fig. S6, ESI†).

Thermo-induced phase transitions of MDAF-4Ln

Compounds **MDAF-4Ln** contain lattice and coordinated water molecules as well as a thermo-responsive dianthracene component in the framework skeleton. It is therefore necessary to investigate their thermal properties. Fig. 3 shows the thermogravimetric (TG) and differential scanning calorimetry (DSC) curves of **MDAF-4Ln**. For **MDAF-4Dy**, a weight loss of 12.8% is observed on heating to 150 °C, corresponding to the removal of ten lattice and two coordinated water molecules (calcd 12.9%). This is followed by a plateau until 210 °C, above which a steep weight loss is found, indicating the decomposition of the organic components and the collapse of the framework structure. The DSC profile shows an endothermic band in the range 30–150 °C peaking at 100 °C with an enthalpy of 249.4 kJ mol^{-1} per formula unit (Fig. 3b), in accordance with the release of water molecules. The IR spectra confirmed that the O–H vibration peaks at 3428 cm^{-1} disappeared at 150 °C (Fig. S7, ESI†). Therefore, the fully dehydrated sample of **MDAF-4Dy** was obtained after thermal treatment at 150 °C for 10 min, which is named **MDAF-4Dy-150**. This phase can convert back to the pristine one by immersing in water for 1 d (Fig. S8–S10, ESI†), indicating that the framework structure of **MDAF-4Dy** is maintained during the dehydration process. Interestingly, an exothermic peak appears at 190 °C in

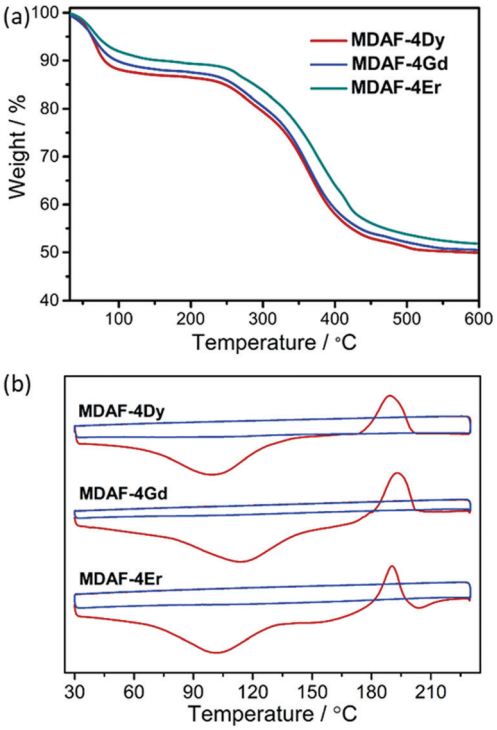

Fig. 3 (a) TG curves and (b) DSC curves of **MDAF-4Ln** with a heating rate of 5 °C min^{-1}. Colour codes in (b): red for the first cycle, blue for the second cycle.

the DSC plot, ascribed to the de-dimerization of the dianthracene ligand. The enthalpy is −109.4 kJ mol^{-1} per formula unit (or −54.7 kJ mol^{-1} per amp$_2$H$_2^{2-}$). Variable temperature IR spectra revealed that peaks at 1281 and 881 cm^{-1} emerged above 180 °C, characteristic of C–H vibrations of de-dimerized anthracene rings (Fig. 4).[59] The new phase, named **MDAF-4Dy-210**, was obtained by heating **MDAF-4Dy** to 210 °C and keeping it at this temperature for 10 min. This new phase shows a different PXRD pattern from that of the pristine one (Fig. S10, ESI†).

For **MDAF-4Gd** and **MDAF-4Er**, their TG and DSC curves are similar to those of **MDAF-4Dy**. They lost the lattice and coordinated water molecules in the temperature range of 30–150 °C

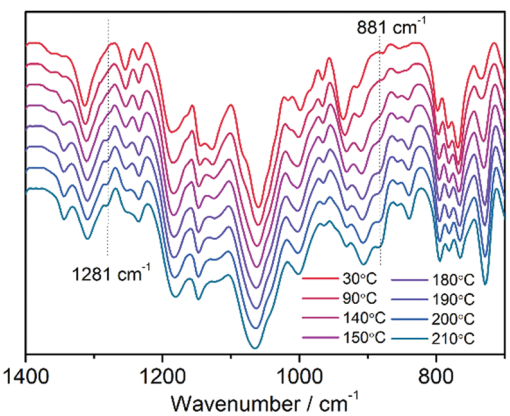

Fig. 4 *In situ* variable temperature infrared spectra of **MDAF-4Dy** measured in the range of 30–210 °C.

(obs. 11.8% and 9.9%, calcd. 11.7% and 9. 8%) (Fig. 3a). The enthalpies are 170.2 kJ mol^{-1} for **MDAF-4Gd** and 141.8 kJ mol^{-1} for **MDAF-4Er** per formula unit (Fig. 3b). Upon further heating, an exothermic peak appeared at 193 °C for **MDAF-4Gd** and at 191 °C for **MDAF-4Er**, associated with the de-dimerization of the dianthracene ligand. The enthalpies are −107.7 and −105.8 kJ mol^{-1} per formula unit, respectively, consistent with that for **MDAF-4Dy**. Apparently, all three compounds of **MDAF-4Ln** underwent two consecutive phase transitions upon heating: first, the release of all water molecules and then, the de-dimerization of the dianthracene moieties. The thermo-induced phase transformations will cause significant changes to their physical properties.

Thermo-triggered change of photophysical properties

Fig. 5a shows the solid-state UV-vis absorption spectra of **MDAF-4Dy**, **MDAF-4Dy-150** and **MDAF-4Dy-210**, translated from the diffuse reflectance spectra using the equation $F(R) = (1 - R)^2/2R$. **MDAF-4Dy** and **MDAF-4Dy-150** show several absorption bands at 210–260 nm, 260–300 nm and 300–450 nm, originating from the n → π* and π → π* transitions of the $amp_2H_2^{2-}$ and oxalate ligands (Fig. 5a and Fig. S11, ESI†). While for **MDAF-4Dy-210**, the peak intensities at the 200–300 nm region are remarkably reduced, which is associated with the de-dimerization of the dianthracene groups. The absorption band at 300–450 nm is also red-shifted to 300–485 nm for **MDAF-4Dy-210**, in agreement with the higher degree of conjugation of anthracene than dianthracene groups. Besides, they all show additional weak peaks around 756 nm, ascribed to the f–f transition of the Dy^{III} ion from the $^6H_{15/2}$ to $^6F_{3/2}$ state.[60]

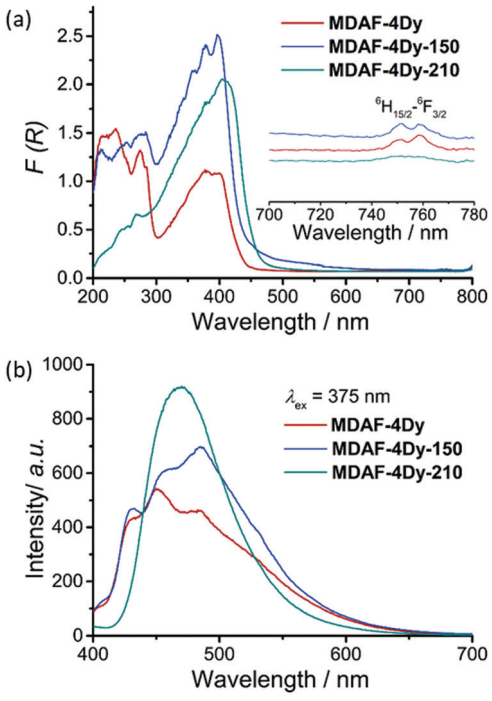

Fig. 5 (a) UV-vis absorption spectra and (b) the steady-state emission spectra excited at 375 nm for **MDAF-4Dy**, **MDAF-4Dy-150** and **MDAF-4Dy-210**. Inset: An enlarged view of the UV-vis absorption spectra of three compounds at 700–780 nm.

Upon excitation at 375 nm, all three compounds show photoluminescence in the visible region. The emission profiles of **MDAF-4Dy** and **MDAF-4Dy-150** are quite similar showing three peaks at 430, 450 and 485 nm (Fig. 5b), attributed to the vibrational manifold of the π* → π transition of dianthracene. The lifetimes are 3.35–4.33 ns and 1.96–2.69 ns for **MDAF-4Dy** and **MDAF-4Dy-150**, respectively (Fig. S12, S13 and Table S6, ESI†). The quantum yields (QY) are 1.22% for **MDAF-4Dy** and 1.49% for **MDAF-4Dy-150**. The smaller QY of the former could be due to the presence of water molecules in **MDAF-4Dy** which facilitate vibrational quenching by O–H oscillators. After de-dimerization, **MDAF-4Dy-210** shows a red-shift and broad emission peak at 470 nm (QY = 7.11%), attributed to the formation of an excimer of the anthracene groups with staggered π−π stacking interactions (average life time τ_{av} = 1.84 ns) (Fig. 5b and Fig. S14, Table S6, ESI†).[36,61]

For compounds **MDAF-4Gd** and **MDAF-4Er**, only the pristine samples were subjected to photophysical property studies. Their absorption spectra in the visible region are similar to those of **MDAF-4Dy** (Fig. S15 and S16, ESI†). For **MDAF-4Er**, characteristic Er^{3+} f–f absorption bands were observed peaking at 488 ($^4I_{15/2}$ → $^4F_{7/2}$), 521 ($^4I_{15/2}$ → $^2H_{11/2}$), 542 ($^4I_{15/2}$ → $^4S_{3/2}$), 653 ($^4I_{15/2}$ → $^4F_{9/2}$) and 804 nm ($^4I_{15/2}$ → $^4I_{9/2}$) (Fig. S16a, ESI†).[60,62] The emission profiles of the two compounds in the visible region are analogous to those of **MDAF-4Dy** (Fig. S15b and S16b, ESI†). The lifetimes are 5.31–5.49 ns for **MDAF-4Gd**, and 4.42–6.33 ns for **MDAF-4Er**, comparable to those for **MDAF-4Dy**. The quantum yields are 11.85% for **MDAF-4Gd**, and 1.11% for **MDAF-4Er** (Fig. S17, S18 and Table S6, ESI†). As the quantum yields of **MDAF-4Dy** and **MDAF-4Er** are much lower than that of **MDAF-4Gd** in the visible region, an efficient energy transfer from the dianthracene ligand to Dy^{III} or Er^{III} ion could occur. Indeed, emission in the NIR region was observed for **MDAF-4Er** around 1536 and 1568 nm (Fig. S19, ESI†), corresponding to the $^4I_{13/2}$ → $^4I_{15/2}$ transition of the Er^{III} ion.

Thermo-triggered change of magnetic properties

The magnetic properties of **MDAF-4Ln**, **MDAF-4Dy-150** and **MDAF-4Dy-210** were studied. At 300 K, the $\chi_M T$ values (per Ln_2 unit) are 28.70, 28.02 and 28.00 cm^3 K mol^{-1} for **MDAF-4Dy**, **MDAF-4Dy-150** and **MDAF-4Dy-210**, respectively, 15.70 cm^3 K mol^{-1} for **MDAF-4Gd** and 22.81 cm^3 K mol^{-1} for **MDAF-4Er** (Fig. S20–S22, ESI†), which agree well with the spin-only value of 28.34 cm^3 K mol^{-1} expected for two Dy^{III} ions ($^6H_{15/2}$, $S = 5/2$, $L = 5$, $g_J = 4/3$), 15.76 cm^3 K mol^{-1} expected for two Gd^{III} ions ($^8S_{7/2}$, $S = 7/2$, $L = 0$, $g_J = 2$), and 22.96 cm^3 K mol^{-1} for two Er^{III} ions ($^4I_{15/2}$, $S = 3/2$, $L = 6$, $g_J = 6/5$). The presence of weak antiferromagnetic (AF) interactions between the lanthanide centres in **MDAF-4Ln** is confirmed by the continuous decreasing of the $\chi_M T$ values of **MDAF-4Gd** upon cooling with a small negative Weiss constant (−0.79 K). Therefore, the progressive decrease of $\chi_M T$ in **MDAF-4Dy** and **MDAF-4Er** upon cooling is due to the combination of the depopulation of the m_J sublevels and weak Ln···Ln AF interactions. Furthermore, the unsaturation of the magnetization and the non-superimposition of the *M vs. H/T* plots support the existence of magnetic anisotropy and/or lower-lying excited states (Fig. S20 and S23, ESI†).[63]

To examine the magnetic dynamics of **MDAF-4Dy** before and after thermal treatment, ac susceptibility measurements were performed. For **MDAF-4Dy**, both the in-phase (χ') and out-of-phase (χ'') components are frequency-dependent under zero dc field (Fig. 6a and Fig. S24, ESI†), characteristic of the SMM behaviour. The Cole–Cole plots can be fit using a generalized Debye model to extract the relaxation time (τ).[64] The α values, which are the coefficients that determine the width of the distribution of relaxation times, fall in the range of 0.27–0.55 in the temperature range of 2–12 K (Table S7, ESI†). The broad range of α values suggests that more than one relaxation process could operate at low temperatures. The best fit of the $\ln\tau$ *vs.* T^{-1} curve can be achieved by considering the Orbach and Quantum tunnelling processes using eqn (1),[65] where U_{eff} represents the energy barrier (Fig. 6d). The parameters are U_{eff} = 41.5 K (28.8 cm^{-1}), $\tau_0 = 2.2 \times 10^{-5}$ s and $\tau_{\text{QTM}} = 0.06$ s.

$$\tau^{-1} = {\tau_{\text{QTM}}}^{-1} + {\tau_0}^{-1} \exp\left(\frac{U_{\text{eff}}}{kT}\right) \quad (1)$$

To better understand the magnetic properties of **MDAF-4Dy**, complete-active-space self-consistent field (CASSCF) calculations on an individual Dy^{III} fragment of complex **MDAF-4Dy** on the basis of X-ray determined geometries have been carried out with MOLCAS 8.4[66] and SINGLE_ANISO[67] programs (see the ESI† for details). The calculated energy levels (cm^{-1}), g (g_x, g_y, g_z) tensors, and the predominant m_J values of the lowest eight KDs of one type of individual Dy^{III} fragment are shown in Table S10 (ESI†). The ground KD is mostly composed of the $m_J = \pm 15/2$ state (Table S11, ESI†). The first excited KD is mixed by several m_J states severely, resulting in a large transversal magnetic moment (Fig. 7). The transversal magnetic moment in the ground KD of **MDAF-4Dy** is only 0.10×10^{-1} μ_B which is small enough for the relaxation to proceed through the first excited state. However, the experimental effective U_{eff} is much smaller than the calculated energy gap between the lowest two KDs of an individual Dy^{III} fragment, attributed to the possible unfavourable effects of anharmonic phonons,[68] Raman magnetic relaxation, quantum tunneling of the magnetization (QTM), and so on, on the energy barrier. Although the magnetic anisotropy of compound **MDAF-4Dy** mainly comes from individual Dy^{III}, the Dy^{III}–Dy^{III} interactions have a considerable influence on its slow magnetic relaxation process.

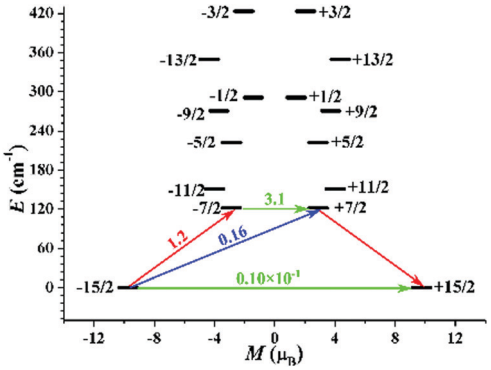

Fig. 7 Magnetization blocking barrier for individual Dy^{III} fragments in **MDAF-4Dy**. The thick black lines represent the KDs of the individual Dy^{III} fragment as a function of their magnetic moment along the magnetic axis. The green lines correspond to the diagonal matrix elements of the transversal magnetic moment. The blue line represents the Orbach relaxation process. The path shown by the red arrows represents the most probable path for magnetic relaxation in the corresponding compounds. The numbers at each arrow stand for the mean absolute value of the corresponding matrix element of transition magnetic moment.

The magnetic susceptibilities of **MDAF-4Dy** were fit by the program POLY_ANISO[67] using the exchange parameters from Table 3. As the calculated ground g_z value of individual Dy^{III} fragment is close to 20, the Dy^{III}–Dy^{III} exchange interactions can be approximately regarded as the Ising type during the fitting (Fig. 8). All parameters were calculated with respect to the pseudo-spin $\tilde{S}$ = 1/2 of the Dy^{III} ions. The total coupling parameters $\tilde{J}_{\text{total}}$ (dipolar and exchange) were included in fitting the magnetic susceptibilities. The calculated and experimental $\chi_M T$ *versus* T plots of **MDAF-4Dy** are shown in Fig. S31 (ESI†), where the fit is close to the experiment at low temperatures, but it has some deviation at high temperatures.[69] The negative values of the total coupling parameter $\tilde{J}_{\text{total}}$ (Table 3) are indicative of the AF Dy^{III}–Dy^{III} interactions in **MDAF-4Dy** within the Lines model.[70] The exchange energies E (cm^{-1}), the energy differences between each exchange doublets Δ_t (cm^{-1}) and the g_z for the lowest eight exchange doublets are all shown in Table S12 (ESI†), where the g_z value of the ground exchange state is 0.000, which confirms the AF interactions between the Dy^{III} ions.

Thermal treatment of **MDAF-4Dy** led to dramatic changes in magnetic dynamics. For **MDAF-4Dy-150**, frequency-dependent ac signals were again observed under zero dc field (Fig. 6b and Fig. S25, ESI†), characteristic of the SMM behaviour.

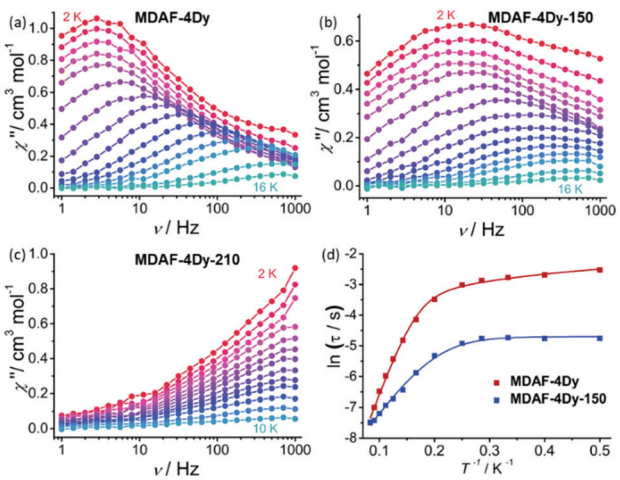

Fig. 6 Frequency dependence of the χ'' signals measured under zero dc field for (a) **MDAF-4Dy**, (b) **MDAF-4Dy-150** and (c) **MDAF-4Dy-210** at the depicted temperatures. (d) Plots of $\ln\tau$ *vs.* T^{-1} for **MDAF-4Dy** and **MDAF-4Dy-150**.

Table 3 Fitted exchange coupling constant $\tilde{J}_{\text{exch}}$, the calculated dipole–dipole interaction $\tilde{J}_{\text{dip}}$ and the total $\tilde{J}_{\text{total}}$ between the Dy^{III} ions in **MDAF-4Dy**. The intermolecular interaction zJ' was fitted to 0.01 cm^{-1}

MDAF-4Dy	$\tilde{J}_{\text{dip}}$	$\tilde{J}_{\text{exch}}$	$\tilde{J}_{\text{total}}$
$\tilde{J}_1$	−0.38	−0.75	−1.13
$\tilde{J}_2$	−2.78	−2.00	−4.78

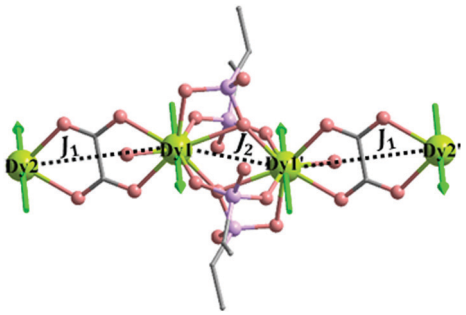

Fig. 8 Scheme of the Dy^{III}–Dy^{III} interactions in **MDAF-4Dy**. The green arrows represent the calculated orientations of the local main magnetic axes on Dy^{III} ions in the ground KDs.

However, the χ'' signals become broader with the peaks moving to higher frequencies. The broad ac signals suggest the presence of multiple relaxation processes. By considering both the Orbach and the Quantum tunnelling processes, the best fit of the $\ln\tau$ *vs.* T^{-1} curve was achieved using eqn (1), giving parameters of U_{eff} = 24.0 K (16.7 cm^{-1}), $\tau_0 = 7.3 \times 10^{-5}$ s and τ_{QTM} = 0.009 s. The ac susceptibilities of the rehydrated sample of **MDAF-4Dy-150-re** were tested, which gave identical profiles to those of **MDAF-4Dy** (Fig. S26, ESI†), and similar parameters of U_{eff} = 39.7 K, $\tau_0 = 2.1 \times 10^{-5}$ s and τ_{QTM} = 0.05 s. The results confirm that the dehydration/rehydration processes of **MDAF-4Dy** are reversible.

For **MDAF-4Dy-210**, frequency-dependent χ'' signals were also observed under zero external field, but without maximum appearing below 1 kHz. The situation was not improved by applying an external field of 500 Oe (Fig. 6c and Fig. S27, ESI†). Therefore, the energy barrier of this phase cannot be estimated.

From the above results, it is clear that all three Dy phases exhibit SMM behaviour under zero dc field. However, the energy barriers decrease in the following order: **MDAF-4Dy** (41.5 K) > **MDAF-4Dy-150** (24.0 K) > **MDAF-4Dy-210** (not available). The energy barrier of **MDAF-4Dy-150** is about half of that of the pristine compound, indicating that the relaxation is accelerated after dehydration. This can be a result of the symmetry reduction of the Dy coordination sphere due to the removal of coordinated water which decreases the magnetic anisotropy. Moreover, the relaxation rate of **MDAF-4Dy-210** is even faster because only tails of χ'' signals were observed at 2 K below 1 kHz. The dissociation of the dianthracene groups in the MOF skeleton may play nontrivial roles in affecting the local geometry of the Dy ions and hence the magnetic dynamics.

For Er compound, only the magnetic properties of pristine **MDAF-4Er** were investigated. Unlike **MDAF-4Dy**, **MDAF-4Er** showed frequency-dependent ac signals only after a dc field was applied. Slow relaxation of magnetization was clearly observed under an optimum field of 1 kOe below 4 K (Fig. S29, ESI†). By assuming that there is only one characteristic relaxation process with one energy barrier and one time constant, the energy barrier can be extracted from eqn (2).[71]

$$\ln\left(\frac{\chi''}{\chi'}\right) = \ln(\omega\tau_0) + \frac{U_{eff}}{kT} \quad (2)$$

A linear fit of the $\ln(\chi''/\chi')$ *versus* T^{-1} curve allows the extraction of the energy barrier (U_{eff}) and pre-exponential factor (τ_0) which are 7.4 K and 3.2×10^{-6} s, respectively (Fig. S29e, ESI†). It is worth mentioning that field-induced slow magnetization relaxation was also observed in a few Er-MOFs with energy barriers below 13.0 K.[22,72,73]

Conclusions

In this study, we report three isostructural Ln-dianthracene compounds $Ln_2(amp_2H_2)_2(C_2O_4)(H_2O)_2{\cdot}xH_2O$ (**MDAF-4Ln**) with three-dimensional open framework structures. The structure is composed of Ln-chains and dianthracence linkages. Although dominant AF interactions were observed between the magnetic centres, **MDAF-4Dy** showed SMM behaviour under zero dc field, which was further rationalized by theoretical calculations. More interestingly, **MDAF-4Dy** experienced two consecutive phase transitions: first, the loss of all lattice and coordinated water molecules and then, the dissociation of dianthracene groups of $amp_2H_2^{2-}$. The thermo-induced structural transformations were accompanied by significant changes in its single-molecule magnetic behaviour and luminescence properties. **MDAF-4Dy** is the first example of the Ln-dianthracene MOFs showing responsive magnetic and luminescence behaviour. This work provides a new route for designing smart magneto-optical bifunctional MOFs for future applications.

Conflicts of interest

There are no conflicts to declare.

Acknowledgements

This work was supported by grants from the National Key R&D Program of China (2017YFA0303203 and 2018YFA0306004) and the National Natural Science Foundation of China (21731003, 21973046).

Notes and references

1 (*a*) G. M. Espallargas and E. Coronado, *Chem. Soc. Rev.*, 2018, **47**, 533–557; (*b*) E. Coronado, *Nat. Rev. Mater.*, 2020, **5**, 87–104.
2 (*a*) J. D. Rinehart and J. R. Long, *Chem. Sci.*, 2011, **2**, 2078–2085; (*b*) Y.-S. Meng, S.-D. Jiang, B.-W. Wang and S. Gao, *Acc. Chem. Res.*, 2016, **49**, 2381–2389; (*c*) C. Gao, A. Genoni, S. Gao, S. Jiang, A. Soncini and J. Overgaard, *Nat. Chem.*, 2020, **12**, 213–219.
3 (*a*) J. C. G. Bünzli and C. Piguet, *Chem. Soc. Rev.*, 2005, **34**, 1048–1077; (*b*) X. Yang, X. Lin, Y. Zhao, Y.-S. Zhao and D. Yan, *Angew. Chem., Int. Ed.*, 2017, **56**, 7853–7857.
4 (*a*) D. N. Woodruff, R. E. P. Winpenny and R. A. Layfield, *Chem. Rev.*, 2013, **113**, 5110–5148; (*b*) Z.-H. Zhu, M. Guo, X.-L. Li and J.-K. Tang, *Coord. Chem. Rev.*, 2019, **378**, 350–364; (*c*) H. Tian and L.-M. Zheng, *Acta Chim. Sin.*, 2020, **78**, 34–55.

5 (*a*) R. J. Blagg, C. A. Muryn, E. J. L. McInnes, F. Tuna and R. E. P. Winpenny, *Angew. Chem., Int. Ed.*, 2011, **50**, 6530–6533; (*b*) J. D. Rinehart, M. Fang, W. J. Evans and J. R. Long, *J. Am. Chem. Soc.*, 2011, **133**, 14236–14239.
6 N. Ishikawa, M. Sugita, T. Ishikawa, S.-Y. Koshihara and Y. Kaizu, *J. Am. Chem. Soc.*, 2003, **125**, 8694–8695.
7 M. A. AlDamen, J. M. Clemente-Juan, E. Coronado, C. Martí-Gastaldo and A. Gaita-Ariño, *J. Am. Chem. Soc.*, 2008, **130**, 8874–8875.
8 S.-D. Jiang, B.-W. Wang, H.-L. Sun, Z.-M. Wang and S. Gao, *J. Am. Chem. Soc.*, 2011, **133**, 4730–4733.
9 Y.-C. Chen, J.-L. Liu, L. Ungur, J. Liu, Q.-W. Li, L.-F. Wang, Z.-P. Ni, L. F. Chibotaru, X.-M. Chen and M.-L. Tong, *J. Am. Chem. Soc.*, 2016, **138**, 2829–2837.
10 P.-B. Jin, Y.-Q. Zhai, K.-X. Yu, R. E. P. Winpenny and Y.-Z. Zheng, *Angew. Chem., Int. Ed.*, 2020, **59**, 9350–9354.
11 C. A. P. Goodwin, F. Ortu, D. Reta, N. F. Chilton and D. P. Mills, *Nature*, 2017, **548**, 439.
12 F.-S. Guo, B. M. Day, Y.-C. Chen, M.-L. Tong, A. Mansikkamäki and R. A. Layfield, *Science*, 2018, **362**, 1400–1403.
13 C. A. Gould, K. R. McClain, J. M. Yu, T. J. Groshens, F. Furche, B. G. Harvey and J. R. Long, *J. Am. Chem. Soc.*, 2019, **141**, 12967–12973.
14 K. Liu, X. Zhang, X. Meng, W. Shi, P. Cheng and A. K. Powell, *Chem. Soc. Rev.*, 2016, **45**, 2423–2439.
15 D. Zeng, M. Ren, S.-S. Bao, J.-S. Feng, L. Li and L.-M. Zheng, *Chem. Commun.*, 2015, **51**, 2649–2652.
16 Z. Chen, B. Zhao, P. Cheng, X.-Q. Zhao, W. Shi and Y. Song, *Inorg. Chem.*, 2009, **48**, 3493–3495.
17 Y.-X. Ren, X.-J. Zheng, L.-C. Li, D.-Q. Yuan, M. An and L.-P. Jin, *Inorg. Chem.*, 2014, **53**, 12234–12236.
18 M. Chen, E. C. Sañudo, E. Jiménez, S.-M. Fang, C.-S. Liu and M. Du, *Inorg. Chem.*, 2014, **53**, 6708–6714.
19 L. Zhang, S. Guan, Y. Fan, C. Du, D. Zhao and B. Liu, *Z. Kristallogr. – Cryst. Mater.*, 2019, **234**, 33–41.
20 C. Bai, C.-T. Li, H.-M. Hu, B. Liu, J.-D. Li and G. Xue, *Dalton Trans.*, 2019, **48**, 814–817.
21 C. Zhang, X. Ma, P. Cen, X. Jin, J. Yang, Y.-Q. Zhang, J. Ferrando-Soria, E. Pardo and X. Liu, *Dalton Trans.*, 2020, **49**, 14123–14132.
22 J. M. Seco, I. Oyarzabal, S. Pérez-Yáñez, J. Cepeda and A. Rodríguez-Diéguez, *Inorg. Chem.*, 2016, **55**, 11230–11248.
23 S. Mohapatra, B. Rajeswaran, A. Chakraborty, A. Sundaresan and T. K. Maji, *Chem. Mater.*, 2013, **25**, 1673–1679.
24 X. Zhang, V. Vieru, X. Feng, J.-L. Liu, Z. Zhang, B. Na, W. Shi, B.-W. Wang, A. K. Powell, L. F. Chibotaru, S. Gao, P. Cheng and J. R. Long, *Angew. Chem., Int. Ed.*, 2015, **54**, 9861–9865.
25 F. Ma, J. Xiong, Y.-S. Meng, J. Yang, H.-L. Sun and S. Gao, *Inorg. Chem. Front.*, 2018, **5**, 2875–2884.
26 Y. Xin, J. Wang, M. Zychowicz, J. J. Zakrzewski, K. Nakabayashi, B. Sieklucka, S. Chorazy and S. I. Ohkoshi, *J. Am. Chem. Soc.*, 2019, **141**, 18211–18220.
27 F. Ma, R. Sun, A.-H. Sun, J. Xiong, H.-L. Sun and S. Gao, *Inorg. Chem. Front.*, 2020, **7**, 930–938.
28 G. Huang, G. Fernandez-Garcia, I. Badiane, M. Camarra, S. Freslon, O. Guillou, C. Daiguebonne, F. Totti, O. Cador, T. Guizouarn, B. Le Guennic and K. Bernot, *Chem. – Eur. J.*, 2018, **24**, 6983–6991.
29 (*a*) O. Cador, B. Le Guennic and F. Pointillart, *Inorg. Chem. Front.*, 2019, **6**, 3398–3417; (*b*) Z. Zhu, X.-L. Li, S. Liu and J. Tang, *Inorg. Chem. Front.*, 2020, **7**, 3315–3326.
30 G. Cosquer, M. Morimoto, M. Irie, A. Fetoh, B. K. Breedlove and M. Yamashita, *Dalton Trans.*, 2015, **44**, 5996–6002.
31 P.-F. Shi, B. Zhao, G. Xiong, Y.-L. Hou and P. Cheng, *Chem. Commun.*, 2012, **48**, 8231–8233.
32 I. Oyarzabal, B. Fernández, J. Cepeda, S. Gómez-Ruiz, A. J. Calahorro, J. M. Seco and A. Rodríguez-Diéguez, *CrystEngComm*, 2016, **18**, 3055–3063.
33 A. A. García-Valdivia, A. Zabala-Lekuona, A. Goñi-Cárdenas, B. Fernández, J. A. García, J. F. Quílez del Moral, J. Cepeda and A. Rodríguez-Diéguez, *Inorg. Chim. Acta*, 2020, **509**, 119687.
34 (*a*) X.-D. Huang, Y. Xu, K. Fan, S.-S. Bao, M. Kurmoo and L.-M. Zheng, *Angew. Chem., Int. Ed.*, 2018, **57**, 8577–8581; (*b*) X.-D. Huang, J.-G. Jia, M. Kurmoo, S.-S. Bao and L.-M. Zheng, *Dalton Trans.*, 2019, **48**, 13769–13779; (*c*) X.-D. Huang, G.-H. Wen, S.-S. Bao, J.-G. Jia and L.-M. Zheng, *Chem. Sci.*, 2021, **12**, 929–937.
35 G. Collet, T. Lathion, C. Besnard, C. Piguet and S. Petoud, *J. Am. Chem. Soc.*, 2018, **140**, 10820–10828.
36 Q. Zou, S.-S. Bao, X.-D. Huang, G.-H. Wen, J.-G. Jia, L.-Q. Wu and L.-M. Zheng, *Chem. – Asian J.*, 2021, DOI: 10.1002/asia.202100283.
37 (*a*) J.-C. Liu, X.-D. Huang, Q. Zou, S.-S. Bao, X.-Z. Wang, J.-Y. Ma and L.-M. Zheng, *J. Mater. Chem. C*, 2020, **8**, 7369–7377; (*b*) Q. Zou, J.-C. Liu, X.-D. Huang, S.-S. Bao and L.-M. Zheng, *Chin. Chem. Lett.*, 2021, **32**, 1519–1522; (*c*) J.-C. Liu, Q. Zou, X.-D. Huang, S.-S. Bao and L.-M. Zheng, *Eur. J. Inorg. Chem.*, 2021, 1565–1570.
38 A. Clearfield and K. Demadis, *Metal Phosphonate Chemistry: From Synthesis to Applications*, The Royal Society of Chemistry, 2012.
39 J.-G. Mao, *Coord. Chem. Rev.*, 2007, **251**, 1493–1520.
40 (*a*) S.-S. Bao, G. K. H. Shimizu and L.-M. Zheng, *Coord. Chem. Rev.*, 2019, **378**, 577–594; (*b*) G.-G. Weng and L.-M. Zheng, *Sci. China: Chem.*, 2020, **63**, 619–636; (*c*) S.-S. Bao, M.-F. Qin and L.-M. Zheng, *Chem. Commun.*, 2020, **56**, 12090–12108.
41 A. D. G. Firmino, F. Figueira, J. P. C. Tomé, F. A. A. Paz and J. Rocha, *Coord. Chem. Rev.*, 2018, 355, 133–149.
42 F.-N. Shi, F. A. Almeida Paz, P. Ribeiro-Claro and J. Rocha, *Chem. Commun.*, 2013, **49**, 11668–11670.
43 (*a*) J. A. Groves, P. A. Wright and P. Lightfoot, *Inorg. Chem.*, 2005, **44**, 1736; (*b*) J. P. S. Mowat, J. A. Groves, M. T. Wharmby, S. R. Miller, Y. Li, P. Lightfoot and P. A. Wright, *J. Solid State Chem.*, 2009, **182**, 2769–2778.
44 C. Serre, N. Stock, T. Bein and G. Férey, *Inorg. Chem.*, 2004, **43**, 3159.
45 D.-K. Cao, S.-Z. Hou, Y.-Z. Li and L.-M. Zheng, *Cryst. Growth Des.*, 2009, **9**, 4445–4449.
46 R. Fu, S. Hu and X. Wu, *Cryst. Growth Des.*, 2014, **14**, 6197–6204.
47 O. Kahn, *Molecular Magnetism*, Wiley-VCH, New York., 1993.

48 SAINT, Program for Data Extraction and Reduction, Siemens Analytical X-ray Instruments, Madison, WI, 1994–1996.
49 SHELXTL (version 5.0), Reference Manual, Siemens Industrial Automation, Analytical Instruments, Madison, WI, 1995.
50 A. L. Spek, *J. Appl. Crystallogr.*, 2003, **36**, 7–13.
51 M. Pinsky and D. Avnir, *Inorg. Chem.*, 1998, **37**, 5575–5582.
52 X. Li, T. Liu, Q. Lin and R. Cao, *Cryst. Growth Des.*, 2010, **10**, 608–617.
53 L. Zhang, S. Xu, Y. Zhou, X. Zheng, C. Yu, Z. Shi, S. U. Hassan and C. Chen, *CrystEngComm*, 2011, **13**, 6511–6519.
54 Y. Zhao, C.-Q. Jiao, Z.-G. Sun, Y.-Y. Zhu, K. Chen, C.-L. Wang, C. Li, M.-J. Zheng, H. Tian, S.-H. Sun and W. Chu, *Cryst. Growth Des.*, 2012, **12**, 3191–3199.
55 T.-H. Yang, D.-K. Cao, Y.-Z. Li and L.-M. Zheng, *J. Solid State Chem.*, 2010, **183**, 1159–1164.
56 L. Liu, Z.-G. Sun, N. Zhang, Y.-Y. Zhu, Y. Zhao, X. Lu, F. Tong, W.-N. Wang and C.-Y. Huang, *Cryst. Growth Des.*, 2010, **10**, 406–413.
57 Y. Zhu, Z. Sun, Y. Zhao, J. Zhang, X. Lu, N. Zhang, L. Liu and F. Tong, *New J. Chem.*, 2009, **33**, 119–124.
58 D. W. Kang, S. E. Ju, D. W. Kim, M. Kang, H. Kim and C. S. Hong, *Adv. Sci.*, 2020, **7**, 2002142.
59 D. J. De Frees, M. D. Miller, D. Talbi, F. Pauzat and Y. Ellinger, *Astrophys. J.*, 1993, **408**, 530–538.
60 K. B. Yatsimirskii and N. K. Davidenko, *Coord. Chem. Rev.*, 1979, **27**, 223–273.
61 X.-D. Huang, M. Kurmoo, S.-S. Bao, K. Fan, Y. Xu, Z.-B. Hu and L.-M. Zheng, *Chem. Commun.*, 2018, **54**, 3278–3281.
62 Y. Xu, S.-S. Bao, X.-D. Huang and L.-M. Zheng, *Cryst. Growth Des.*, 2018, **18**, 4045–4053.
63 K. L. M. Harriman, J. L. Brosmer, L. Ungur, P. L. Diaconescu and M. Murugesu, *J. Am. Chem. Soc.*, 2017, **139**, 1420–1423.
64 K. S. Cole and R. H. Cole, *J. Chem. Phys.*, 1941, **9**, 341–351.
65 G. Brunet, R. Marin, M.-J. Monk, U. Resch-Genger, D. A. Gálico, F. A. Sigoli, E. A. Suturina, E. Hemmer and M. Murugesu, *Chem. Sci.*, 2019, **10**, 6799–6808.
66 F. Aquilante, J. Autschbach, R. K. Carlson, L. F. Chibotaru, M. G. Delcey, L. D. Vico, I. F. Galván, N. Ferré, L. M. Frutos, L. Gagliardi, M. Garavelli, A. Giussani, C. E. Hoyer, G. Li Manni, H. Lischka, D. Ma, P. Å. Malmqvist, T. Müller, A. Nenov, M. Olivucci, T. B. Pedersen, D. Peng, F. Plasser, B. Pritchard, M. Reiher, I. Rivalta, I. Schapiro, J. Segarra-Martí, M. Stenrup, D. G. Truhlar, L. Ungur, A. Valentini, S. Vancoillie, V. Veryazov, V. P. Vysotskiy, O. Weingart, F. Zapata and R. Lindh, *J. Comput. Chem.*, 2016, **37**, 506–541.
67 (*a*) L. F. Chibotaru, L. Ungur and A. Soncini, *Angew. Chem., Int. Ed.*, 2008, **47**, 4126–4129; (*b*) L. Ungur, W. Van den Heuvel and L. F. Chibotaru, *New J. Chem.*, 2009, **33**, 1224–1230; (*c*) L. F. Chibotaru, L. Ungur, C. Aronica, H. Elmoll, G. Pilet and D. Luneau, *J. Am. Chem. Soc.*, 2008, **130**, 12445–12455.
68 A. Lunghi, F. Totti, R. Sessoli and S. Sanvito, *Nat. Commun.*, 2017, **8**, 14620.
69 S. K. Langley, D. P. Wielechowski, V. Vieru, N. F. Chilton, B. Moubaraki, B. F. Abrahams, L. F. Chibotaru and K. S. Murray, *Angew. Chem., Int. Ed.*, 2013, **52**, 12014–12019.
70 M. E. Lines, *J. Chem. Phys.*, 1971, **55**, 2977–2984.
71 P. Mondal, B. Dey, S. Roy, S. P. Bera, R. Nasani, A. Santra and S. Konar, *Cryst. Growth Des.*, 2018, **18**, 6211–6220.
72 A. J. Calahorro, I. Oyarzabal, B. Fernández, J. M. Seco, T. Tian, D. Fairen-Jimenez, E. Colacio and A. Rodríguez-Diéguez, *Dalton Trans.*, 2016, **45**, 591–598.
73 L. H. G. Kalinke, D. Cangussu, M. Mon, R. Bruno, E. Tiburcio, F. Lloret, D. Armentano, E. Pardo and J. Ferrando-Soria, *Inorg. Chem.*, 2019, **58**, 14498–14506.

